Neurobiology of Disease

Disrupting Epileptiform Activity by Preventing Parvalbumin Interneuron Depolarization Block

Alexandru Călin, Andrei S. Ilie, and Colin J. Akerman
Department of Pharmacology, University of Oxford, Oxford OX1 3QT, United Kingdom

Inhibitory synaptic mechanisms oppose epileptic network activity in the brain. The breakdown in this inhibitory restraint and propagation of seizure activity has been linked to the overwhelming of feedforward inhibition, which is provided in large part by parvalbumin-expressing (PV) interneurons in the cortex. The underlying cellular processes therefore represent potential targets for understanding and preventing the propagation of seizure activity. Here we use an optogenetic strategy to test the hypothesis that depolarization block in PV interneurons is a significant factor during the loss of inhibitory restraint. Depolarization block results from the inactivation of voltage-gated sodium channels and leads to impaired action potential firing. We used focal NMDA stimulation to elicit reproducible epileptiform discharges in hippocampal organotypic brain slices from male and female mice and combined this with targeted recordings from defined neuronal populations. Simultaneous patch-clamp recordings from PV interneurons and pyramidal neurons revealed epileptiform activity that was associated with an overwhelming of inhibitory synaptic mechanisms and the emergence of a partial, and then complete, depolarization block in PV interneurons. To counteract this depolarization block, we developed protocols for eliciting pulsed membrane hyperpolarization via the inhibitory opsin, archaerhodopsin. This optical approach was effective in counteracting cumulative inactivation of voltage-gated channels, maintaining PV interneuron action potential firing properties during the inhibitory restraint period, and reducing the probability of initiating epileptiform activity. These experiments support the idea that depolarization block is a point of weakness in feedforward inhibitory synaptic mechanisms and represents a target for preventing the initiation and spread of seizure activity.

Key words: **epilepsy; GABAergic; hippocampus; inhibition; optogenetic; seizure**

Significance Statement

$GABA_A$ receptor-mediated synaptic transmission opposes seizure activity by establishing an inhibitory restraint against spreading excitation. Parvalbumin-expressing (PV) interneurons contribute significantly to this inhibitory restraint, but it has been suggested that these cells are overwhelmed as they enter a state of "depolarization block." Here we test the importance of this process by devising an optogenetic strategy to selectively relieve depolarization block in PV interneurons. By inducing brief membrane hyperpolarization, we show that it is possible to reduce depolarization block in PV interneurons, maintain their action potential firing in the face of strong excitation, and disrupt epileptiform activity in an *in vitro* model. This represents a proof of principle that targeting rate-limiting processes can strengthen the inhibitory restraint of epileptiform activity.

Introduction

The disrupted interplay between excitation and inhibition within neuronal networks has long been implicated in seizure pathophysiology. Pharmacological blockade of synaptic inhibition promotes epileptic activity (Curtis et al., 1970; Dichter and Ayala, 1987) and when inhibitory restraint of network activity fails, spatially clustered excitatory pyramidal neurons are recruited to epileptiform events (Cammarota et al., 2013). Feedforward mechanisms and GABA-releasing interneurons represent the cellular components that mediate inhibitory restraint (Trevelyan et al., 2006, 2007), whereby feedforward recruitment of local interneurons serves to prevent synaptic excitation from spreading outward from hyperexcitable parts of the network (Schevon et al., 2012; Trevelyan and Schevon, 2013).

Previous research has suggested that parvalbumin-expressing (PV) interneurons play a central role in this inhibitory restraint

Received Apr. 27, 2020; revised Sep. 21, 2021; accepted Sep. 26, 2021.

Author contributions: A.C., A.S.I., and C.J.A. designed research; A.C. performed research; A.C. analyzed data; A.C., A.S.I., and C.J.A. wrote the paper.

The research leading to these results has received funding from the European Research Council (ERC) under the European Community's Seventh Framework Program FP7/2007-2013, ERC Grant Agreement 617670. A.C. was supported by a Wellcome Trust Doctoral Fellowship (102364/Z/13/Z). A.S.I. was supported by a Junior Research Fellowship in Medical Sciences from University College Oxford.

The authors declare no competing financial interests.

Correspondence should be addressed to Colin J. Akerman at colin.akerman@pharm.ox.ac.uk.

https://doi.org/10.1523/JNEUROSCI.1002-20.2021

(Losi et al., 2010; Cammarota et al., 2013; Sessolo et al., 2015; Parrish et al., 2019). PV interneurons comprise a large proportion of perisomatic-targeting interneurons, including basket cells and axoaxonic cells, and have been shown to play a crucial role in synchronizing network activity in the hippocampus and across cortex (Somogyi and Klausberger, 2005). While other interneuron populations are recruited and contribute to inhibitory restraint mechanisms (Khoshkhoo et al., 2017; Parrish et al., 2019), the dense axonal branching and postsynaptic targeting of PV interneurons (Freund and Buzsáki, 1996), combined with their high and synchronous firing patterns (Galarreta and Hestrin, 1999; Gibson et al., 1999), is thought to underlie the ability of PV interneurons to mediate powerful inhibitory effects.

The cellular processes that lead to a breakdown in inhibitory restraint represent important targets for understanding and disrupting the propagation of seizure activity. A number of possible presynaptic mechanisms have been hypothesized. For example, previous work has indicated that seizure-like activity may be triggered by exhaustion of presynaptic GABA release, as the releasable pool of GABA-containing vesicles becomes depleted (Zhang et al., 2012). Others meanwhile have reported that interneurons can enter a state of depolarization block, which is concurrent with the onset of seizure-like activity and characterized by a cessation in action potential (spiking) output (Dichter and Spencer, 1969; Ziburkus et al., 2006; Cammarota et al., 2013).

Depolarization block occurs during periods of strong or maintained membrane depolarizations and reflects the reduced availability of voltage-gated sodium channels as a result of channel inactivation mechanisms (Rudy, 1978; Fleidervish et al., 1996; Vilin and Ruben, 2001). Fast sodium channel inactivation shows rapid onset on membrane depolarization and underlies the absolute refractory period for spiking (Hodgkin and Huxley, 1952). Meanwhile, slowly developing and longer-lasting sodium channel inactivation emerges with sustained membrane depolarizations, generates cumulative action potential adaptation, and also contributes to depolarization block (Fleidervish et al., 1996; Jung et al., 1997; Qian et al., 2014). These mechansims can combine to induce states of partial depolarization block and ultimately total depolarization block, which is marked by the cessation of spiking. In both cases, recovery from the underlying channel inactivation depends on membrane hyperpolarization (Hodgkin and Huxley, 1952; Fleidervish et al., 1996; Jung et al., 1997).

Here we use an optogenetic strategy to directly investigate the functional significance of PV interneuron depolarization block in an *in vitro* hippocampal model of seizure-like activity. Targeted recordings reveal that genetically identified PV interneurons are strongly recruited as part of endogenous feedforward inhibitory restraint. However, in the face of sustained excitation, PV interneurons show evidence of depolarization block processes, which culminate in complete spike failure around the initiation of epileptiform activity. Using pulsed light activation of a hyperpolarizing opsin, we are able to selectively reduce the effects of this depolarization block, such that PV interneurons are better able to maintain their action potential firing despite strong network excitation. This results in a greater capacity to counteract epileptiform activity and supports the idea that depolarization block represents a point of weakness in feedforward inhibitory synaptic mechanisms.

Materials and Methods

Preparation of organotypic hippocampal brain slices. All animal work was conducted in accordance with the Animals (Scientific Procedures) Act, 1986 (UK) and under project and personal licenses approved by the Home Office (UK). Previous work has established that hippocampal organotypic slices represent an experimentally accessible model of epileptogenesis (Dyhrfjeld-Johnsen et al., 2010; Berdichevsky et al., 2012; Călin et al., 2018). Organotypic slices have been shown to retain fundamental features of the circuit, including appropriate distributions of interneurons and distinct subcellular targeting of pyramidal neurons (Streit et al., 1989; De Simoni et al., 2003; Di Cristo et al., 2004; Călin et al., 2018). At the stages studied here, glutamatergic and GABAergic synaptic transmission, including chloride homeostasis, are mature (Streit et al., 1989; De Simoni et al., 2003; Ilie et al., 2012). Organotypic hippocampal brain slice cultures, referred to as "brain slices" or "slices," were prepared from 5- to 7-d-old male and female transgenic mice, as described by Stoppini et al. (1991). These mice were either heterozygous or homozygous PV-Cre mice (B6;129P2-Pvalb$^{tm1(cre)Arbr}$/J), purchased from The Jackson Laboratory. All reagents were purchased from Sigma-Aldrich, unless stated otherwise. The whole brain was extracted and transferred into cold (4°C) dissection media containing Earle's balanced salt solution with $CaCl_2$ and $MgSO_4$ (Thermo Fisher Scientific), supplemented with 25.5 mM HEPES, 36.5 mM D-glucose, and 5 mM NaOH. The hemispheres were separated, and the individual hippocampi were dissected and immediately sectioned into 400-μm-thick slices on a McIlwain tissue chopper (Mickle). Cold dissection media was then used to rinse slices before placing them onto sterile, porous Millicell-CM membranes. Slices were maintained in culture for 2–8 weeks in media containing 78.8% (v/v) minimum essential media with GlutaMAX-I (Thermo Fisher Scientific), 20% (v/v) heat-inactivated horse serum (Thermo Fisher Scientific), 1% (v/v) B27 (Thermo Fisher Scientific), 30 mM HEPES, 26 mM D-glucose, 5.8 mM $NaHCO_3$, 1 mM $CaCl_2$, and 2 mM $MgSO_4 \cdot 7\ H_2O$. Brain slices were incubated at 35.5–36°C in a 5% CO_2 humidified incubator.

Viral transduction of brain slices. The organotypic hippocampal brain slices afforded efficient delivery of genetic constructs via visually guided injections of floxed adeno-associated virus (AAV) vectors. After 3–5 d in culture, brain slices were transduced with Cre-dependent AAVs (serotypes 5 and 8) encoding a double-floxed sequence for the light-driven outward proton pump, archaerhodopsin (Arch), fused to enhanced green fluorescent protein [Arch-GFP; either archaerhodopsin-3 under the CBA promoter (Chow et al., 2010); University of Pennsylvania Gene Therapy Program Vector Core, Philadelphia, PA; or ArchT under the CAG promoter (Han et al., 2011); University of North Carolina Gene Therapy Center Vector Core, Chapel Hill, NC]. Transduction was achieved by injecting viral particles (mixed with 1% w/v fast-green for visualization) into 5–10 locations along the pyramidal cell layer of the hippocampus into each brain slice. Fine injection pipettes were pulled from glass capillaries (outer diameter, 1.2 mm; inner diameter, 0.69 mm; Warner Instruments) using a horizontal puller (model P-97, Sutter Instrument). Pipettes were mounted on a manual manipulator (Narishige) and monitored under a microscope (model S6E, Leica) coupled with an external fiber optic light source (100×; Photonic CLS, Leica). A Picospritzer II system (General Valve) delivered controlled pressure pulses (5–10 psi for 1 s) to facilitate slow diffusion of the viral solution into the tissue. Typical titers were $\sim 10^{12}$ IU/ml and injection volumes were ~250 nl/slice. Previous work established that this transduction protocol produces good specificity and efficiency in targeting PV interneurons (Călin et al., 2018). Feeding media was supplemented with 1% (v/v) antibiotic and antimycotic solution (with 10,000 U of penicillin, 10 mg of streptomycin, and 25 μg of amphotericin B/ml) for up to two feeding sessions after injection. Brain slices were allowed at least 2 weeks for expression before being used. Images of Arch-GFP-expressing tissue were captured with an LSM 880 Confocal Microscope equipped with 488 nm lasers and controlled via the ZEN software (Zeiss); or with a camera (Mightex) mounted on the epifluorescence electrophysiology rig.

Electrophysiological recordings. Brain slices were transferred to a submerged recording chamber and maintained at 28°C throughout recordings. The chamber was continuously superfused with artificial CSF (aCSF) containing the following (in mM): NaCl (120), KCl (3), $MgCl_2$ (0.5–1.5), $CaCl_2$ (2–3), NaH_2PO_4 (1.2), $NaHCO_3$ (23), D-glucose (11), and ascorbic acid (0.2). Osmolarity was adjusted to 290 mOsm, and pH was adjusted to 7.36 with NaOH. Oxygen and pH levels were stabilized

by bubbling the aCSF with 95% O_2 and 5% CO_2. Neurons within the hippocampal formation were visualized under transmitted or epifluorescence light using 10× and 60× water-immersion microscope objectives and appropriate filter cubes (model BX51WI, Olympus), and were targeted for single-patch or dual-patch whole-cell or cell-attached recordings. Patch pipettes with tip resistance of 4–9 MΩ were pulled from filamental borosilicate glass capillaries with an outer diameter of 1.2 mm and an inner diameter of 0.69 mm (Warner Instruments), using a horizontal puller (model P-97, Sutter Instrument). Patch pipettes were filled with a K-gluconate internal solution (134 mM K-gluconate, 2 mM NaCl, 10 mM HEPES, 2 mM Na_2ATP, 0.3 mM NaGTP, and 2 mM MgATP), which had been prepared to a pH of 7.36 using KOH, and an osmolarity of 290 mOsm. Before use, the internal solution was filtered with a 0.22 μm syringe filter (Merck Millipore). Pipettes were mounted to a headstage (CV-7b, Molecular Devices) and controlled via a Multiclamp 700B amplifier (Molecular Devices). Pipette capacitance compensation (fast and slow) was applied during voltage-clamp recordings. Pipette capacitance neutralization was not applied during current-clamp recordings. Recordings were low-pass filtered online at 2 kHz (eight-pole Bessel), acquired using Clampex software (pClamp 10, Molecular Devices), and exported into MATLAB (version R2017a; MathWorks) for offline analysis using custom-made scripts. In some experiments, depolarization block was elicited in whole-cell recordings from single PV interneurons by somatic injection of 1-s-long positive current steps, delivered in 50 pA increments. The depolarization block threshold was defined as the first current level at which the PV interneuron spiking terminated during the step. Changes in spike amplitude during current steps were determined by using a least-squares linear fitting method, after excluding the first and final three spikes. Spikes were identified using the *findpeaks* function in MATLAB, and their amplitudes were determined from local maxima and minima in the filtered membrane potential (high-pass, zero-phase, first-order Butterworth filter at 200 Hz). Spike amplitudes were only ever compared in relative terms within the same recording.

Epileptiform discharge model. The *in vitro* electrographic equivalent of seizures is referred to as "epileptiform discharges" (EDs). Organotypic hippocampal brain slices can exhibit spontaneous EDs (Dyhrfjeld-Johnsen et al., 2010; Ellender et al., 2014). In the current study, however, it was essential that the experimenter had temporal control of the EDs, so that timed manipulations could be delivered during the period preceding ED onset. We therefore used an NMDA-evoked seizure model based on previous work, which has been shown to recruit inhibitory restraint mechanisms (Losi et al., 2010, 2016). To induce EDs, local puffs of NMDA (1 mM in aCSF) were delivered via a patch pipette positioned over the CA3 region and connected to a Picospritzer III system (General Valve). For each brain slice, the number and timing of NMDA puffs was adjusted to reliably trigger an ED on each trial. Any slice that exhibited significant levels of spontaneous EDs was not used and, in the small number of cases where a spontaneous seizure occurred during the recording of NMDA-evoked EDs (~5%), these traces were removed from subsequent analyses.

A semiautomated detection algorithm was used to identify the start and end of individual EDs. ED onset was characterized by a pronounced membrane potential depolarization on which high-frequency discharges occurred. First, the signal recorded in current-clamp mode was low-pass filtered at 5 Hz using a zero-phase, first-order Butterworth filter. The start of the ED was defined as the time at which the filtered membrane potential exceeded a threshold of 20 mV above the resting membrane potential (RMP) of the cell, where RMP was defined as the mean membrane potential during the 5 s preceding the first NMDA puff. To determine the end of each ED, a baseline threshold was defined as the RMP of the cell, plus 2 SDs of the signal used to calculate the RMP. Subsequently, the raw voltage trace was low-pass filtered at 0.05 Hz using a zero-phase, first-order Butterworth filter, and the end of the ED defined as the time when the filtered signal first reached the baseline threshold. To detect action potentials during cell-attached recordings, traces were filtered (high-pass, zero-phase, first-order Butterworth filter at 100 Hz), spikes were identified using the *findpeaks* function in MATLAB, and their amplitudes were determined from local maxima and minima in the root mean square of the signal. Spike amplitudes were only ever compared in relative terms, within the same recording.

Optogenetic manipulation. Photoactivation of Arch was achieved by wide-field illumination of the brain slice using a green light-emitting diode (LED; 530 nm peak; Luxeon) placed directly under the slice. Light pulses were 5 ms in duration and delivered at 50 Hz using an external electrical stimulator (Grass S48, Grass Medical Instruments) coupled to an LED power controller. Light power measured at the brain slice was 10.2 mW/mm^2, which equates to delivering <1 mW of laser light via an optic fiber (200 μm fiber tip; 0–400 μm beneath the fiber tip; Stujenske et al., 2015). Even when delivered in continuous mode, any thermal effects associated with this light intensity are below a level that has been shown to modulate neuronal activity (Stujenske et al., 2015; Owen et al., 2019). Furthermore, the pulsed Arch protocol adopted here had a duty cycle of 25% (on, 5 ms; off, 15 ms), meaning that the tissue was exposed to fourfold less light than an equivalent continuous light protocol (Stujenske et al., 2015).

Experimental design and statistical analysis. Digital signal processing and presentation were performed using custom-made programs in the MATLAB environment (version R2017b; MathWorks). Figures were built using vector-based graphic design in CorelDraw (version X6; Corel) and the statistical software GraphPad Prism (version 6.01; GraphPad Software). Data are presented as the mean ± SEM. Statistical tests are reported at the relevant points, along with the test statistic, degrees of freedom, p value (using GraphPad Prism and MATLAB), and the number of recordings, cells, and slices that contributed. Nonparametric tests were used when the data were not normally distributed. Appropriate *post hoc* tests were used when ANOVAs confirmed a statistically significant effect. A χ^2 statistic was used to test whether data shown as time histograms were uniformly distributed. Linear regressions were performed to assess whether trends were significant. Pearson correlations were used to determine similarity between EDs.

Results

Inhibitory synaptic restraint mechanisms are recruited by NMDA-evoked epileptiform discharges

To study inhibitory synaptic restraint, we used an NMDA-evoked seizure model based on previous work by Losi et al. (2010, 2016). NMDA was delivered focally to the CA3 area of organotypic hippocampal brain slices, with the aim of promoting strong local excitation, which ultimately transitions into long-lasting epileptiform events that recruit the entire network. Simultaneous whole-cell patch-clamp recordings from a local pyramidal neuron within the CA3 region, and a distant pyramidal neuron in the CA1 region (~1 mm from the NMDA focus), confirmed that EDs could be evoked under these conditions. The EDs occurred with a delay following NMDA application and, once initiated, were clearly observed as highly synchronous events across the network (Fig. 1*A*). These current-clamp recordings also revealed that excitatory and inhibitory synaptic networks were strongly recruited during the period before ED onset (i.e., the "pre-ED" period). Following NMDA application, the membrane potential of pyramidal neurons exhibited high-frequency, low-amplitude oscillations, consistent with the recruitment of intense excitatory and inhibitory subthreshold synaptic activity, which increased from the early pre-ED period (−20 to −10 s before ED onset) to the late pre-ED period (−10 to 0 s before ED onset; Fig. 1*A*). Voltage-clamp recordings from CA1 pyramidal neurons (at a holding potential of −60 mV, between the reversal potential for glutamatergic and GABAergic currents) confirmed that the neurons received intense barrages of inhibitory currents during the period before ED onset. These inhibitory synaptic currents were ultimately overcome by increasing excitatory currents, leading to the onset of epileptiform activity (Fig. 1*B*). These observations are consistent with the previously

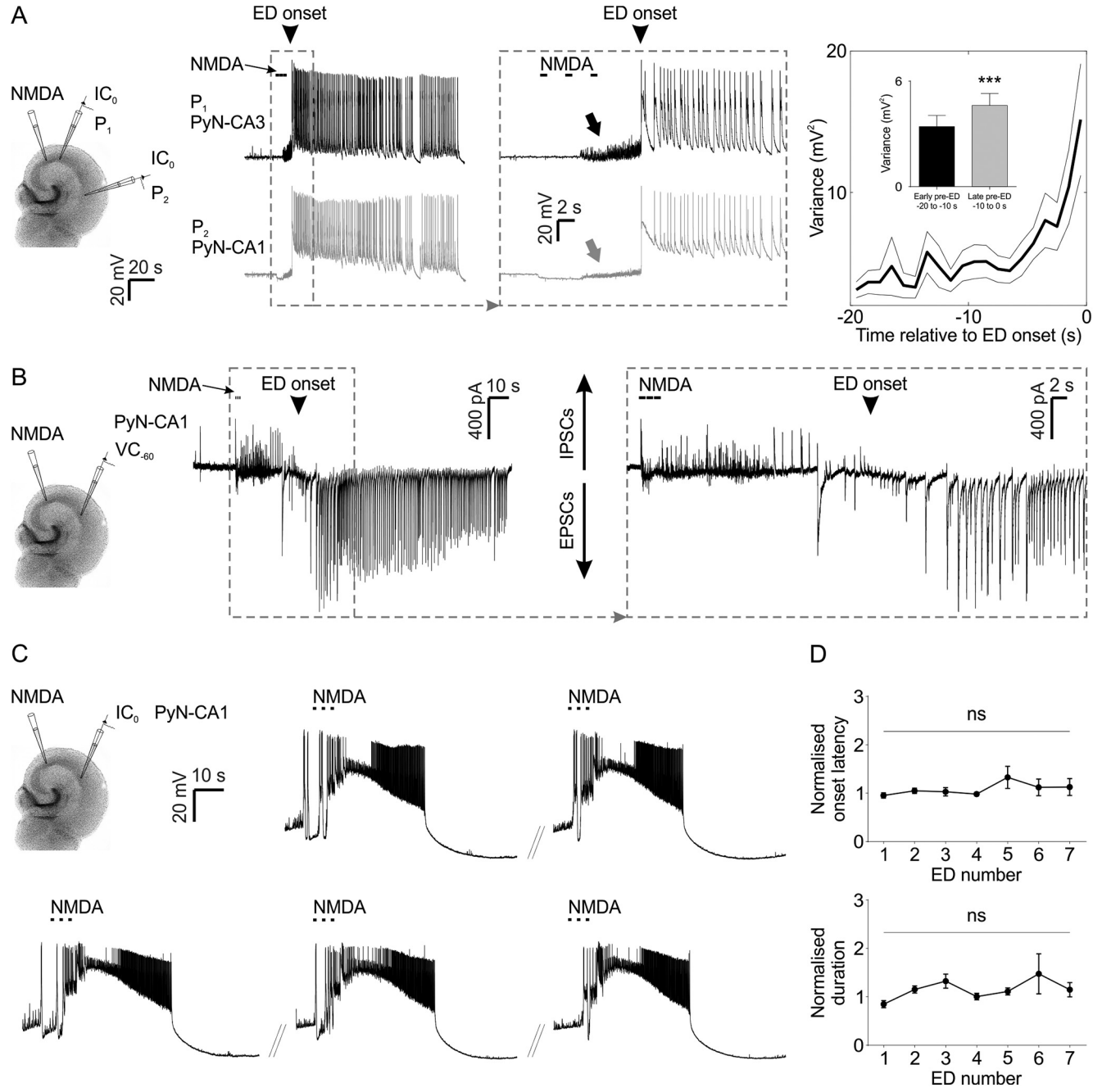

Figure 1. Inhibitory restraint mechanisms are recruited by NMDA-evoked epileptiform discharges. ***A***, Left, Experimental setup showing focal delivery of NMDA to the CA3 region of the hippocampal slice, while pairs of pyramidal neurons (PyN) were recorded simultaneously in current-clamp mode (IC) from the CA3 and CA1 regions. P_1 = patch-clamp recording 1, P_2 = patch-clamp recording 2. Middle, Example recordings and expanded region show a synchronous ED onset (black arrowhead) in the two pyramidal neurons. Black bars indicate NMDA puffs. Subthreshold, high-frequency oscillations in membrane potential (arrows) are evident before ED onset. Right, Variance plot reveals a progressive increase in subthreshold membrane potential variance over the 20 s preceding ED onset. Subthreshold membrane potential variance was higher during the late pre-ED period (before ED onset, −10 to 0 s) than during the early pre-ED period (before ED onset, −20 to −10 s; inset: $N = 36$ EDs, from 12 cells across 12 slices; $W_{(36)} = 81$; $p < 0.0001$; two-tailed matched-pairs Wilcoxon signed-rank test). ***B***, Example voltage-clamp recording (VC) from a CA1 pyramidal neuron shows the transition from intense inhibitory synaptic inputs (upward deflections) to net excitatory currents (downward deflections) around the time of ED onset (black arrowhead). ***C***, Example CA1 pyramidal neuron recording showing consistent and long-lasting EDs evoked by focal NMDA delivery. ***D***, EDs were highly reproducible in terms of relative onset latency (top; $F_{(6,43)} = 1.27$, $p = 0.29$, one-way ANOVA) and duration (bottom; $F_{(6,43)} = 2.0$, $p = 0.09$, one-way ANOVA; $N = 9$ cells across 9 slices). Each measure was normalized to the mean of the first two EDs. ***$p < 0.001$. ns = not significant.

well described phenomenon of feedforward inhibition (Trevelyan et al., 2006, 2007) and validated our model for the study of inhibitory restraint mechanisms in the run-up to epileptiform activity.

To determine the threshold for initiating EDs, the NMDA pulse duration, pressure, and/or number was gradually increased until the first ED was evoked. Once these parameters were established, NMDA was delivered at 5 min intervals to assess the reproducibility of the model. Using this method, EDs were reliably evoked and no failures were observed, even when NMDA applications were made to the same slice over extended periods of time (up to 150 min; Fig. 1*C*, example). Quantitative analysis of 50 EDs from nine experiments revealed a mean ED onset latency of 13.2 ± 1 s from the time of the first NMDA pulse, and a mean ED duration of 36.4 ± 4.8 s. Although ED length and

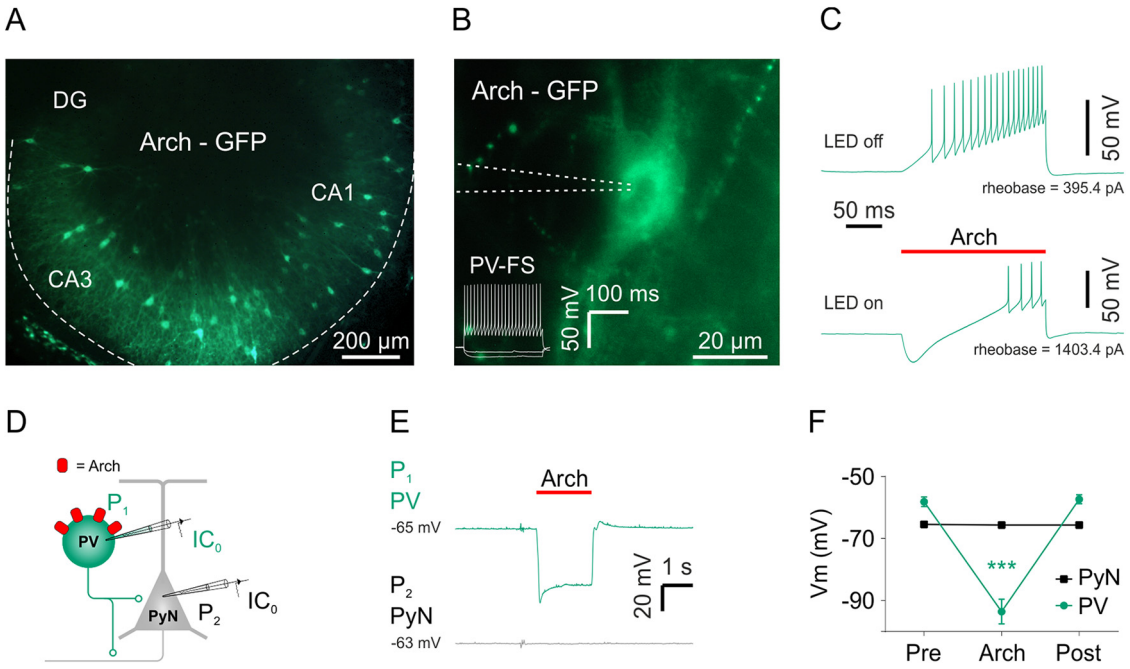

Figure 2. Selective targeting of PV interneurons. ***A***, Low-power image of an organotypic hippocampal brain slice from a PV-Cre mouse, 2 weeks following injection with a double-floxed AAV encoding the light-driven outward proton pump Arch-GFP. ***B***, Arch-GFP-expressing neurons were targeted for electrophysiological recording and, in all cases, exhibited intrinsic properties associated with fast-spiking PV interneurons (inset, PV-FS; $N = 17$ of 17). ***C***, The fast-spiking activity of Arch-GFP-expressing PV interneurons was modulated during the presentation of light from an LED (530 nm peak, "LED on"). ***D***, To confirm selective targeting, simultaneous recordings were performed from neuronal pairs comprising an Arch-GFP-expressing PV interneuron and a nearby nonexpressing pyramidal neuron (PyN). P_1 = patch-clamp recording 1, P_2 = patch-clamp recording 2. ***E***, In all cases, the PV interneuron exhibited a hyperpolarizing response to light, while the pyramidal neuron showed no response. ***F***, Population data confirmed that the PV interneurons exhibit light-induced hyperpolarization, whereas nonexpressing pyramidal neurons exhibit no light response ($F_{(2,30)} = 98.49$, $p < 0.0001$, two-way repeated-measures ANOVA interaction between cell type and timing condition; $p < 0.0001$ for Arch versus Pre (before Arch) and for Arch versus Post (after Arch) at Sidak's multiple-comparisons test; $N = 16$ recordings, from 5 neuronal pairs across 5 slices). ***$p < 0.001$.

latency varied between recordings, the parameters of the repeatedly evoked EDs were highly consistent within the same slice (Fig. 1*D*). Statistical analysis did not reveal any significant variation in onset latency or duration across multiple EDs, confirming the reproducibility of the model.

PV interneurons show strong recruitment and enter depolarization block before the onset of epileptiform discharges

PV interneurons have been strongly implicated in inhibitory restraint mechanisms (Losi et al., 2010; Cammarota et al., 2013; Parrish et al., 2019). To target PV interneurons, we used slices prepared from PV-Cre mice in which Cre recombinase is expressed downstream of the PV promoter sequence. To both visualize PV interneurons and ultimately manipulate the PV interneuron population optically, we delivered floxed AAV vectors encoding the light-driven outward proton pump Arch-GFP (see Materials and Methods). As predicted, Arch-GFP exhibited membrane-localized expression in soma and neuronal processes throughout the pyramidal cell layer of the CA regions, where PV interneurons primarily reside and their axons target the axosomatic compartment of pyramidal neurons (Pawelzik et al., 2002; Bartos and Elgueta, 2012; Fig. 2*A*). To confirm expression in PV interneurons, Arch-GFP-expressing soma were targeted for electrophysiological recordings. In all cases, the neurons exhibited intrinsic properties associated with fast-spiking PV interneurons, and their spiking activity could be modulated by the presentation of light (530 nm peak wavelength; Fig. 2*B*,*C*). To further establish selective expression, recordings were performed from neuronal pairs comprising an Arch-GFP-expressing PV interneuron and a nearby nonexpressing pyramidal neuron (Fig. 2*D*). In all cases, the PV interneuron exhibited a hyperpolarizing response to light, while the simultaneously recorded pyramidal neurons never showed a response to light (Fig. 2*E*,*F*). These data confirmed the selective expression of the AAV in PV interneurons and that light stimulation did not elicit off-target effects in nonexpressing neurons.

To characterize the recruitment of PV interneurons during EDs, we used dual-patch recordings to target pairs of neurons in the CA1 region comprising a labeled PV interneuron and a nearby pyramidal neuron (Fig. 3*A*). As above, EDs were initiated by focal NMDA delivery to the CA3 region, and the PV interneurons were recorded in cell-attached mode to preserve cellular integrity. These experiments confirmed that PV interneurons are powerfully recruited during the inhibitory restraint period, with PV interneuron spiking levels increasing over the pre-ED period (Fig. 3*B*). However, ED onset was characterized by a cessation in PV interneuron spiking and the initiation of intense spiking in the nearby pyramidal neuron (Fig. 3*B*). This buildup in PV interneuron spiking and then the switch from PV interneuron spiking to pyramidal neuron spiking were general features across EDs (Fig. 3*C*). And plotting spike counts for the two neuronal populations around the time of ED onset confirmed a close inverse relationship between PV interneuron spiking and pyramidal neuron spiking (Fig. 3*D*). This pattern of strong PV interneuron recruitment during the period of inhibitory restraint, which culminates in a cessation in PV interneuron spiking, matched previous reports that PV interneurons enter a period of total depolarization block at the onset of EDs (Ziburkus et al., 2006; Cammarota et al., 2013).

Before the cessation in spiking associated with total depolarization block, membrane depolarization can produce cumulative

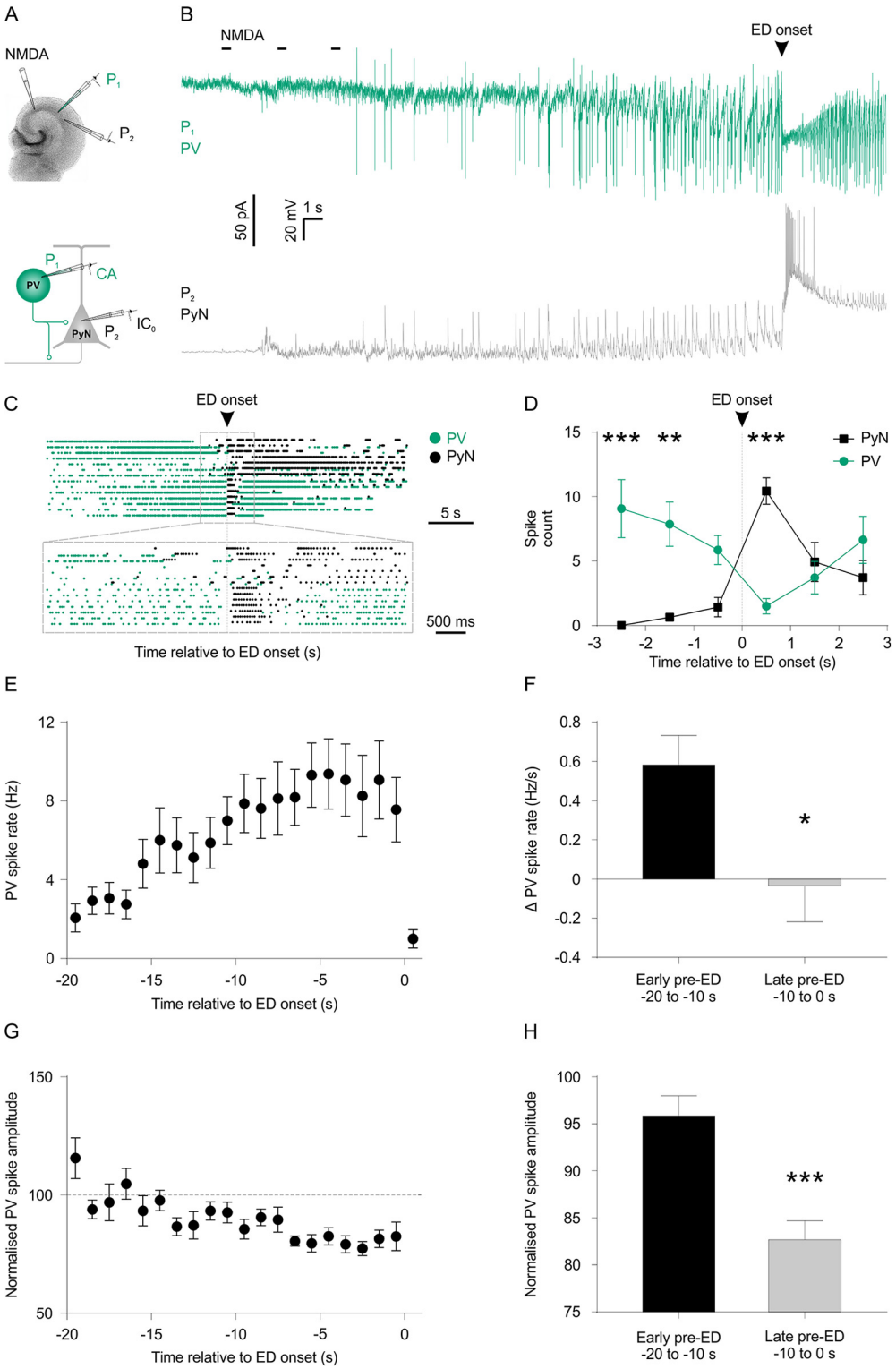

Figure 3. PV interneurons enter depolarization block before an epileptiform discharge. ***A***, Left, Experimental setup showing simultaneous recordings from a PV interneuron in cell-attached mode (CA) and a pyramidal neuron (PyN) in whole-cell current-clamp mode (IC), while EDs were initiated by focal NMDA delivery to the CA3 region. P_1 = patch-clamp recording 1, P_2 = patch-clamp recording 2. ***B***, Example recording showing that PV interneuron spiking was strongly recruited during the pre-ED inhibitory restraint period, but ceased at ED onset (black arrowhead), when spiking commenced in the pyramidal neuron. ***C***, Raster plots of PV interneuron spikes (green) and pyramidal neuron spikes (black), shown at a lower (top) and higher (bottom) time resolution. Each row shows the spikes recorded during a different ED, plotted relative to the time of ED onset (black arrowhead). Across EDs, PV interneuron spiking is recruited strongly during the pre-ED inhibitory restraint period, which ceases around ED onset as spiking commences in the pyramidal neuron ($N = 14$ EDs, from three neuronal pairs across three slices). ***D***, Spike count plotted around the time of ED onset (arrowhead at 0 s) confirms a close inverse relationship between PV interneuron spiking and pyramidal neuron spiking ($F_{(5,65)} = 12.73$, $p < 0.0001$, two-way repeated-measures ANOVA interaction between cell type and time; Sidak's multiple-comparisons test, PyN vs PV: $p < 0.0001$ at -2.5 s and at 0.5 s; $p = 0.0012$ at -1.5 s; $p = 0.1053$ at -0.5; $p = 0.9861$ at 1.5 s; and $p = 0.5181$ at 2.5 s; $N = 14$ EDs, from 3 neuronal pairs across 3 slices). ***E***, During the pre-ED period, the PV interneuron spike rate tended to increase, before exhibiting an abrupt drop at ED onset (slope = 0.36 ± 0.06; $R^2 = 0.11$; $N = 16$ EDs, from three cells across three slices; $F_{(1,316)} = 40.6$, $p < 0.0001$, linear regression of pre-ED data). ***F***, In the 10 s before ED onset ("Late pre-ED"), PV interneurons showed a lower increase in spike rate compared with earlier in the inhibitory restraint period ("Early pre-ED"; 20–10 s

adaptation effects on spike rates and amplitudes, which are also associated with voltage-gated sodium channel inactivation (Fleidervish et al., 1996; Jung et al., 1997; Qian et al., 2014). We therefore examined the pre-ED period more closely, to see whether there was further evidence of partial depolarization block. Over the course of the pre-ED period, the PV interneuron spike rate increased (Fig. 3*E*) and membrane potential measurements in pyramidal neurons indicated that PV interneuron spikes continued to be associated with postsynaptic hyperpolarizing effects (mean: at 15 s before ED onset, -2.2 ± 0.2 mV; at 5 s before ED onset, -1.8 ± 0.4 mV). However, while the PV interneuron spiking rate rose over the pre-ED period, there was a reduction (i.e., slowing) in the increase in spike rate from 0.58 ± 0.15 Hz/s at 15 s before ED onset to -0.03 ± 0.18 Hz/s at 5 s before ED onset ($N = 16$ EDs, from three cells across three slices: $W_{(16)} = 27$, $p = 0.0335$, two-tailed Wilcoxon matched-pairs signed-rank test; Fig. 3*F*). On the same timescale, there was also a significant reduction in the normalized PV interneuron spike amplitude from $96 \pm 2\%$ at 15 s before ED onset to $83 \pm 2\%$ at 5 s before ED onset ($N = 14$ EDs, from three cells across three slices: $W_{(14)} = 0$, $p = 0.0001$, two-tailed Wilcoxon matched-pairs signed-rank test; Fig. 3*G*,*H*). These data are consistent with there being a cumulative inactivation of voltage-gated sodium channels in PV interneurons during the inhibitory restraint period, which is initially evident as a partial depolarization block and ultimately culminates in total depolarization block around ED onset.

An optogenetic strategy can recover PV interneurons from depolarization block

Since recovery from sodium channel inactivation depends on membrane hyperpolarization, we hypothesized that it should be possible to counteract PV interneuron depolarization block by invoking brief hyperpolarizing currents. To achieve this, we adopted an optogenetic strategy based on the pulsed activation of Arch (Chow et al., 2010; Han et al., 2011). PV interneurons were transduced with floxed Arch-GFP AAVs in brain slices from PV-Cre mice and allowed 3–4 weeks for expression, as above. Brief membrane hyperpolarizations could then be selectively induced in the PV interneurons by delivering trains of green light pulses (5 ms duration at 50 Hz; i.e., 5 ms "on," 15 ms "off").

First, we assessed the potential of light-evoked hyperpolarizations to counteract depolarization block induced by somatic current injection. Arch-expressing PV interneurons were recorded in current-clamp and received 1-s-duration steps of positive somatic current injection in 50 pA increments. The threshold for total depolarization block was defined as the lowest current step at which spiking activity failed (Fig. 4*A*). Under control conditions without light, depolarization block was evident as there was a pronounced drop in PV interneuron spike number from 118.6 ± 21.2 to 45.4 ± 6.8, with a 50 pA increment in somatic current injection ($N = 8$ PV interneurons across three slices; $t_{(7)} = 3.83$, $p = 0.0064$, two-tailed paired t test; Fig. 4*A*,*B*). In an attempt to counteract this depolarization block, the same somatic current injections were delivered, but now with brief membrane hyperpolarizations elicited via activation of Arch (Fig. 4*A*). In line with our prediction, the light-evoked hyperpolarizations significantly reduced the depolarization block. For the same levels of somatic current injection, the hyperpolarizing Arch pulses were able to maintain the mean PV interneuron spike numbers at 98.6 ± 17.0 and 97.8 ± 19.1 ($N = 8$ PV interneurons across three slices; $t_{(7)} = 0.12$, $p = 0.91$, two-tailed paired t test; Fig. 4*A*, *C*). This represented more than a twofold increase in PV interneuron spiking at the threshold for depolarization block. The reduction in sodium channel inactivation was also evident in spike amplitudes. Under control conditions, somatic current injection caused spike amplitudes to decrease at a rate of $63.0 \pm 22.4\%$/s ($N = 8$ PV interneurons across three slices; $t_{(7)} = 2.45$, $p = 0.04$, two-tailed paired t test; Fig. 4*A*,*B*). However, when hyperpolarizing brief Arch pulses were delivered, PV interneuron spike amplitude remained much more stable, decreasing at a rate of only $7 \pm 2.7\%$/s for the same somatic current injection ($N = 8$ PV interneurons across three slices; $t_{(7)} = 1.01$, $p = 0.35$, two-tailed paired t test; Fig. 4*A*,*C*). For current injections below the threshold for depolarization block, pulsed Arch did not significantly affect the mean spike rate of PV interneurons across the 1 s step. At these levels of current injection, spike numbers without light pulses were 109.8 ± 17.9 and comparable to spike numbers with pulsed Arch activation of 99.7 ± 21.2 ($N = 8$ PV interneurons across three slices; $t_{(7)} = 1.48$, $p = 0.18$, two-tailed paired t test).

As predicted, the trains of Arch pulses rescued PV interneuron spiking levels from depolarization block by inducing a brief hyperpolarizing effect during the "light-on" phase of the pulse train, enabling greater spiking during the "light-off" phase (Fig. 4*D*). In addition, and consistent with these observations representing a relief from depolarization block, we found no evidence that the Arch pulses elicited intrinsic rebound spiking in the PV interneurons, when recorded in either whole-cell current-clamp configuration or cell-attached configuration (Fig. 4*E*, *F*). These data establish that an optogenetic strategy for eliciting brief hyperpolarizing pulses can successfully attenuate the impact of depolarization block and offers the potential to increase the inhibitory output of PV interneurons.

Attenuating depolarization block increases PV interneuron spiking during the recruitment of inhibitory restraint

We next investigated whether the same optogenetic strategy could be used to boost PV interneuron spiking during the period of inhibitory restraint that precedes the onset of EDs. To do this, we performed simultaneous recordings from a CA1 pyramidal neuron and a nearby Arch-expressing PV interneuron, and then delivered NMDA focally to the CA3 region (Fig. 5*A*). The occurrence of EDs was determined from the activity of the pyramidal neuron recorded in current-clamp mode. As described above, NMDA application resulted in the recruitment of PV interneurons under control conditions (i.e., no Arch activation). However, we observed that this recruitment in PV interneuron spiking could be significantly enhanced with our optical strategy for attenuating depolarization block. Eliciting brief membrane hyperpolarizations via trains of Arch pulses (5 ms duration at 50 Hz) increased PV interneuron spiking during the inhibitory restraint period (Fig. 5*A*–*C*). The initial recruitment of PV interneurons was similar, but as the period of inhibitory restraint

←

before ED onset; $N = 16$ EDs, from three cells across three slices; $W_{(16)} = 27$, $p = 0.03$, two-tailed Wilcoxon matched-pairs signed-rank test). Delta spike rates were averaged over a 10 s period, using 1 s time bins. ***G***, During the pre-ED period, PV interneuron spike amplitude tended to decrease (slope = -0.01; $R^2 = 0.16$; $N = 14$ EDs, from three cells across three slices; $F_{(1,247)} = 46.31$, $p < 0.0001$, linear regression of pre-ED data). Spike amplitudes were normalized to the mean of the first 10 recorded spikes. ***H***, PV interneuron spike amplitude was significantly smaller in the late pre-ED period than in the early pre-ED period ($N = 14$ EDs, from three cells across three slices; $W_{(14)} = 0$, $p = 0.0001$, two-tailed Wilcoxon matched-pairs signed-rank test). *$p < 0.05$, ***$p < 0.001$.

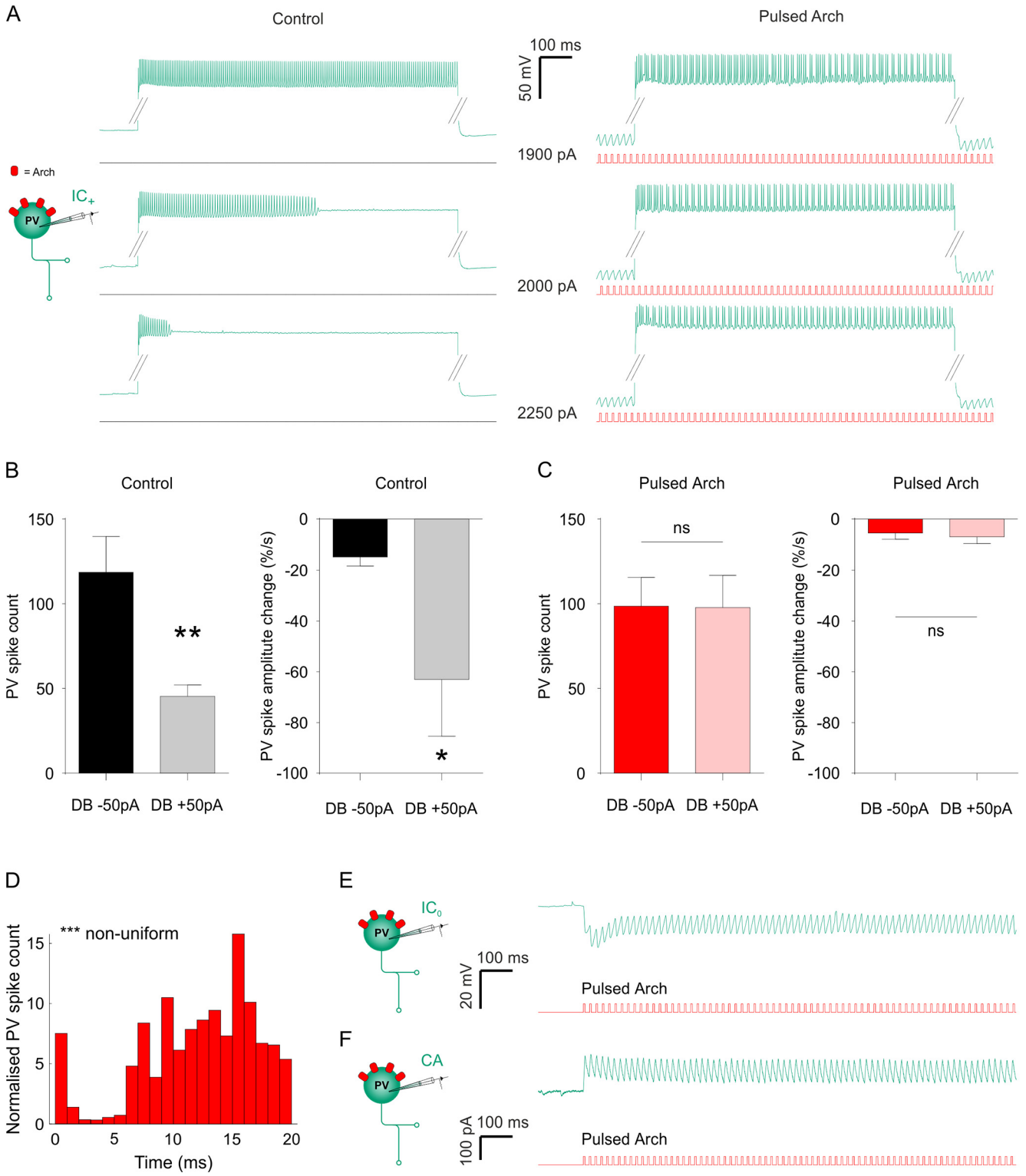

Figure 4. An optogenetic strategy for recovering PV interneurons from depolarization block. ***A***, Left, Cartoon showing PV interneurons expressing Arch, which were targeted for current-clamp recordings (IC). Recordings from the same PV interneuron (right) across three increasing levels of somatic current injection (top to bottom) under either control conditions without light (left), or with pulsed activation of Arch (right; 5 ms duration at 50 Hz; i.e., 5 ms on, 15 ms off). ***B***, Under control conditions, a 50 pA increment in somatic current injection elicited a pronounced drop in PV interneuron spike number at the threshold for depolarization block (left; $N = 8$ PV interneurons; $t_{(7)} = 3.84$, $p = 0.006$, two-tailed paired t test) and a decrease in spike amplitude (right; $t_{(7)} = 2.45$, $p = 0.04$, two-tailed paired t test; $N = 8$ PV interneurons from three slices). Spike amplitude change was calculated from a linear fit of spike amplitudes and expressed as a percentage change per second (see Materials and Methods). ***C***, At the same level of somatic current injection as in ***B***, Arch pulses prevented the decrease in PV interneuron spike number (left; $t_{(7)} = 0.12$, $p = 0.90$, two-tailed paired t test) and prevented the rundown in spike amplitude (right; $t_{(7)} = 1.01$, $p = 0.35$, two-tailed paired t test; $N = 8$ PV interneurons from three slices). $^*p < 0.05$, $^{**}p < 0.01$. ***D***, Distribution of PV interneuron spike times plotted relative to the light pulse. Light was on for 0–5 ms and off for 5–20 ms. Data are from all current steps. Spike count was normalized by the number of current steps and cells recorded (eight steps from eight PV interneurons across three slices). The distribution of PV interneuron spike times was nonuniform ($\chi^2_{(14,5384)} = 1034.1$, $p < 0.0001$). $^{***}p < 0.001$. ***E***, Light pulses did not elicit intrinsic rebound spiking when PV interneurons were recorded in whole-cell current-clamp configuration and without somatic current injection ($N = 9$ PV interneurons across four slices). ***F***, Light pulses did not elicit intrinsic rebound spiking when PV interneurons were recorded in cell-attached configuration ($N = 3$ PV interneurons across three slices). ns = not significant.

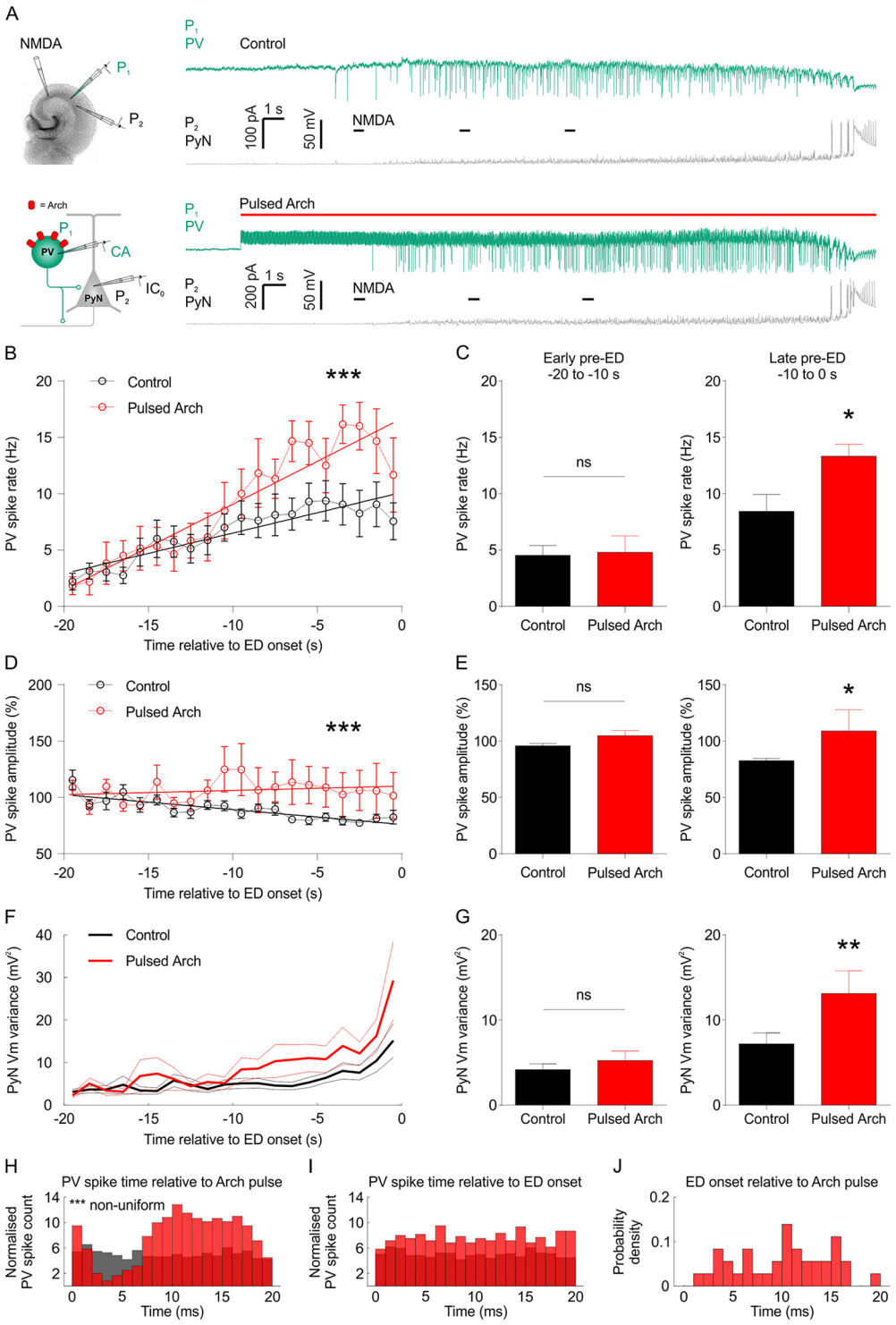

Figure 5. Preventing depolarization block increases PV interneuron output during periods of inhibitory restraint. ***A***, Left, Experimental setup showing simultaneous recordings of an Arch-expressing PV interneuron in cell-attached mode (CA) and pyramidal neuron (PyN) in whole-cell current-clamp mode (IC), while EDs were initiated by focal NMDA application to the CA3 region. P_1 = patch-clamp recording 1, P_2 = patch-clamp recording 2. Right, Traces show an example dual recording of a PV interneuron (green) and a pyramidal neuron (gray) during the period of inhibitory restraint before ED onset under control conditions without light (top) or when the PV interneuron received pulsed activation of Arch (bottom; 5 ms duration at 50 Hz). ***B***, PV interneuron spiking increased with pulsed Arch ($N = 14$ EDs during control; $N = 6$ EDs during Arch pulses; from three neuronal pairs across three slices; $F_{(1,434)} = 14.94$, $p = 0.0001$, ANCOVA between conditions). ***C***, Pulsed Arch did not affect the PV interneuron spike rate during the early pre-ED period (left; $U_{(16,6)} = 46.5$, $p = 0.93$, two-tailed Mann–Whitney test; $N = 14$ EDs during control and $N = 6$ EDs during Arch pulses, from three neuronal pairs across three slices), but increased PV interneuron spike rate during the late pre-ED period (right; $U_{(16,6)} = 17.5$, $p = 0.02$, two-tailed Mann–Whitney test). ***D***, Pulsed Arch maintained PV interneuron spike amplitude compared with controls ($N = 14$ EDs during control; $N = 6$ EDs during Arch pulses; from three neuronal pairs across three slices; $F_{(1,354)} = 11.3$, $p = 0.0009$, ANCOVA between conditions). Spike amplitudes were normalized to the mean of the first 10 recorded spikes. ***E***, Pulsed Arch did not alter spike amplitude during the early pre-ED period (left; $t_{(18)} = 2.03$, $p = 0.06$, two-tailed unpaired t test; $N = 14$ EDs during control; $N = 6$ EDs during Arch pulses; from three neuronal pairs across three slices), but increased PV interneuron spike amplitude during the late pre-ED period (right; $t_{(18)} = 2.14$, $p = 0.047$, two-tailed unpaired t test). ***F***, Variance plots of the subthreshold membrane potential of the pyramidal neuron over the 20 s preceding ED onset. ***G***, Pulsed Arch activation of the PV interneurons did not alter the subthreshold membrane potential of the pyramidal neuron during the early pre-ED period (left; 4.2 ± 0.7 mV^2 control; vs 5.2 ± 1.1 mV^2 pulsed Arch; $t_{(76)} = 0.5138$, $p = 0.6089$, two-tailed unpaired t test corrected for multiple comparisons;

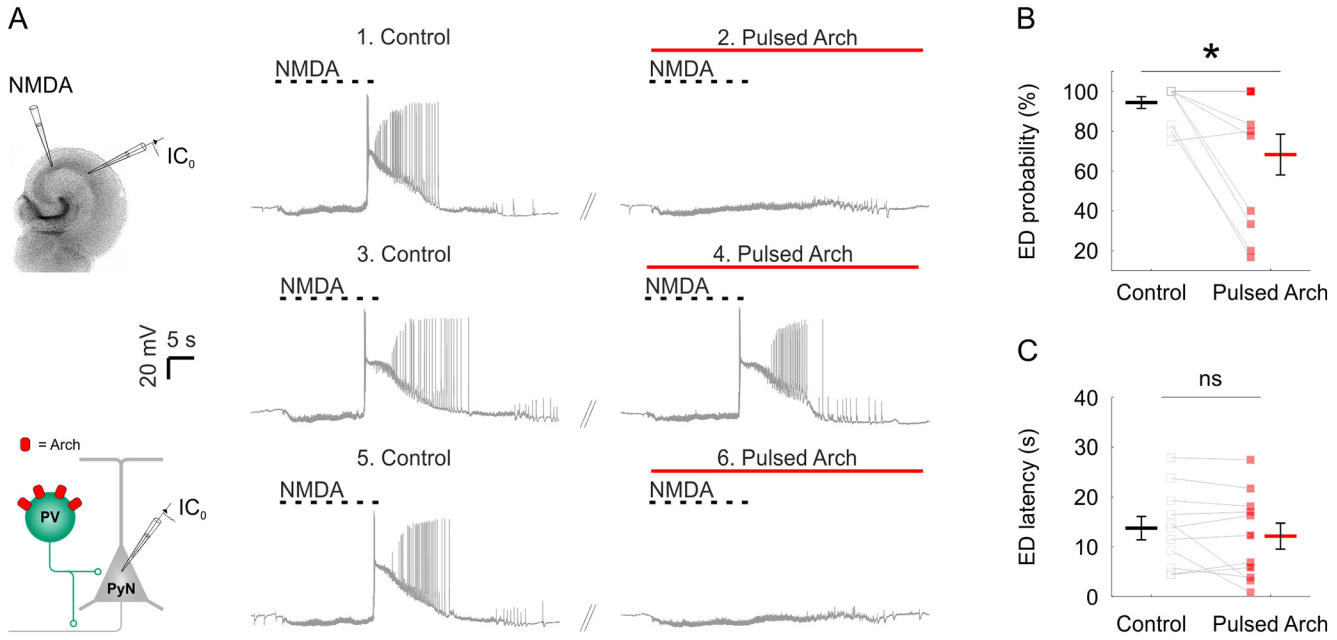

Figure 6. Attenuating PV interneuron depolarization block reduces the probability of epileptiform discharges. ***A***, Left, Experimental setup in which PV interneurons expressed Arch and current-clamp recordings (IC) from pyramidal neurons were used as a readout of EDs, elicited by focal NMDA delivery to the CA3 region. Right, Traces show six (1 → 6) NMDA applications in the same slice, at 5 min intervals, and alternated between control trials without light (left; 1, 3, and 5) and trials with pulsed Arch activation (right; 2, 4, and 6; 5 ms duration at 50 Hz, red bar). Under control conditions, each NMDA application evoked an ED. However, in trials where Arch was pulsed in PV interneurons during the period of inhibitory restraint, EDs often failed to initiate. Black bars indicate NMDA puffs. ***B***, Pulsed Arch led to a reduction in the probability of an ED ($N = 11$ cells across 11 slices; $W_{(7)} = 1$, $p = 0.0313$, two-tailed matched-pairs Wilcoxon signed-rank test). ***C***, ED onset time (i.e., latency) relative to the start of the NMDA protocol was similar for control EDs and EDs that did occur under the pulsed Arch protocol ($W_{(11)} = 27$, $p = 0.6377$, two-tailed matched-pairs Wilcoxon signed-rank test; $N = 11$ cells across 11 slices). *$p < 0.05$. ns = not significant.

continued, Arch-pulsed PV interneurons showed a more sustained increase in spiking, such that their spike frequency continued to increase at an overall mean rate of 0.76 ± 0.08 Hz/s compared with 0.36 ± 0.06 Hz/s in controls ($N = 16$ and 6 EDs, from three cells across three slices; $F_{(1,434)} = 14.94$, $p = 0.0001$, ANCOVA between conditions; Fig. 5*B*). Consequently, the Arch-pulsed PV interneurons reached higher mean spike rates of 13.3 ± 1.1 Hz compared with 8.4 ± 1.5 Hz in controls, across the late pre-ED period ($N = 16$ and 6 EDs, from three cells across three slices; $U_{(16,6)} = 17.5$, $p = 0.0222$, two-tailed Mann–Whitney test; Fig. 5*C*).

Further evidence that Arch pulses attenuated depolarization block was that PV interneurons no longer showed a reduction in spike amplitude over the course of the inhibitory restraint period, consistent with less cumulative inactivation of voltage-gated sodium channels ($N = 14$ and 6 EDs, from three cells across three slices; $F_{(1,354)} = 11.258$, $p = 0.0009$, ANCOVA between conditions; Fig. 5*D*). As a result, PV interneuron spike amplitude was higher during the late pre-ED period when Arch was pulsed, compared with controls when Arch was not pulsed ($109.0 \pm 18.9\%$ vs $82.7 \pm 2.0\%$; $N = 14$ and 6 EDs, from three cells across three slices; $t_{(18)} = 2.136$, $p = 0.047$, two-tailed unpaired *t* test; Fig. 5*E*). The greater recruitment of PV interneurons was also evident in the subthreshold membrane potential fluctuations recorded in the nearby pyramidal neurons, consistent with a greater recruitment of inhibitory restraint against increasing excitatory input (Fig. 5*F*). As a result, the subthreshold membrane potential variance of the pyramidal neuron was greater during the late pre-ED period when Arch was pulsed (control, 7.2 ± 1.3 mV^2; vs pulsed Arch, 13.1 ± 2.7 mV^2; $N = 24$ and 16 EDs, from 12 cells across 12 slices; $t_{(76)} = 2.84$, $p = 0.0058$, two-tailed unpaired *t* test corrected for multiple comparisons; Fig. 5*G*). As in the current injection experiments (Fig. 4*D*), the Arch pulses rescued PV interneuron spiking during the pre-ED period by inducing a brief hyperpolarizing effect during the light-on phase of the pulse train, enabling greater spiking during the light-off phase (Fig. 5*H*). The increases in spiking levels were therefore associated with millisecond shifts in spike timing, although this did not appear to be related to ED timing, as there was no relationship among PV interneuron spikes, Arch pulses, and ED onset on this timescale (Fig. 5*I*,*J*).

Attenuating PV interneuron depolarization block reduces the probability of epileptiform discharges

Having established that light-induced hyperpolarizations can attenuate PV interneuron depolarization block during inhibitory restraint, we systematically investigated the impact on EDs. To this end, EDs were evoked by NMDA application to the CA3 region and monitored via current-clamp recordings from distal

←

$N = 24$ and 16 EDs, from 12 cells across 12 slices), but increased subthreshold membrane potential of the pyramidal neuron during the late pre-ED period (right; 7.2 ± 1.3 mV^2 control; vs 13.1 ± 2.7 mV^2 pulsed Arch; $t_{(76)} = 2.84$, $p = 0.0058$, two-tailed unpaired *t* test corrected for multiple comparisons). ***H***, Histogram of PV interneuron spike times aligned to the Arch pulses (on for 0–5 ms; off for 5–20 ms) during the late pre-ED period. Overlapping data show a normalized spike count for controls without light (gray data) and when Arch was pulsed (red data; the distribution of PV interneuron spike times was nonuniform ($\chi^2_{(14,795)} = 94.2$, $p < 0.0001$). Spike count was normalized by the number of EDs (14 EDs recorded from three PV interneurons across three slices). ***I***, Histogram of PV interneuron spike times aligned to ED onset (at 0 ms on the *x*-axis). The distribution of PV interneuron spike times was not different to a uniform distribution ($\chi^2_{(19,914)} = 13.9$, $p = 0.7883$; 14 EDs recorded from three PV interneurons across three slices). ***J***, Histogram of ED onset times, aligned to the Arch pulses (on for 0–5 ms; off for 5–20 ms; the distribution of ED onset times was not different to a uniform distribution ($\chi^2_{(1,36)} = 1$, $p = 0.3173$; 36 EDs recorded from 10 PV interneurons across 10 slices). The distribution of ED onset times did not differ between the first and second halves of the 20 ms cycle time for Arch pulses ($p = 0.6177$, binomial test). *$p < 0.05$, **$p < 0.01$, ***$p < 0.001$. ns = not significant.

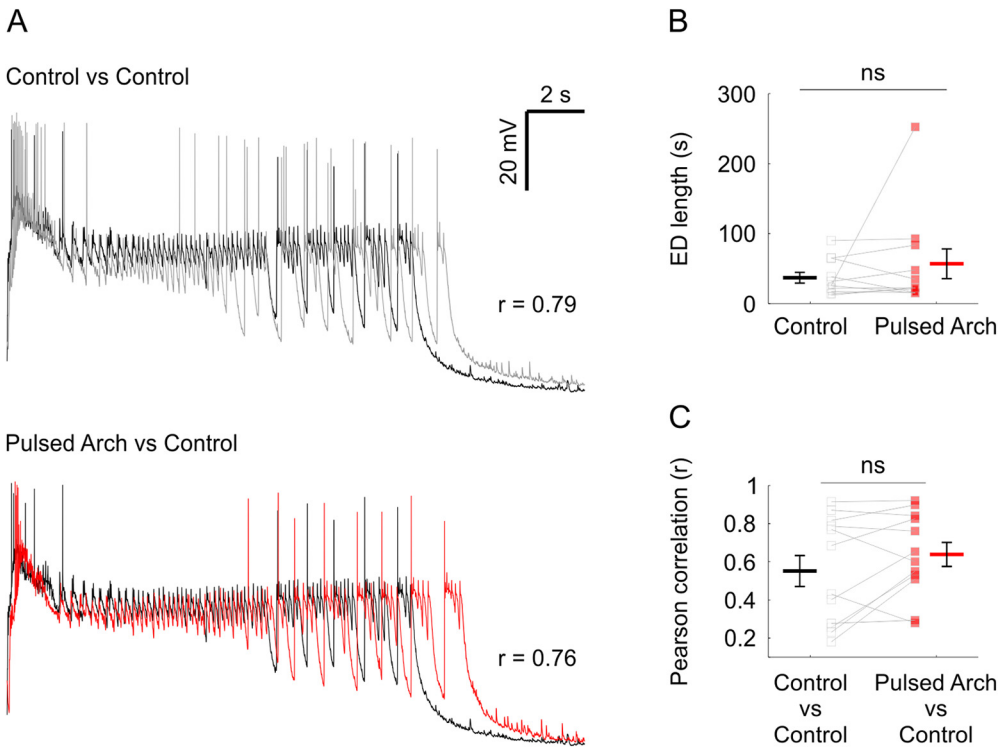

Figure 7. The morphology of epileptiform discharges remains stable. ***A***, Top, Control EDs recorded from the same hippocampal slice exhibited similar duration and morphology, as indicated by their high correlation coefficient. Bottom, For EDs that occurred under the pulsed Arch protocol, their duration and morphology were similar to control EDs recorded in the same slice. ***B***, ***C***, For EDs observed under the pulsed Arch protocol, ED length was not different to controls ($W_{(11)} = 25$, $p = 0.5195$, two-tailed matched-pairs Wilcoxon signed-rank test; $N = 11$ cells across 11 slices; ***B***), nor was the correlation in ED morphologies ($t_{(11)} = 1.723$, $p = 0.1128$, two-tailed paired t test; $N = 12$ pairs across 12 slices; ***C***). ns = not significant.

pyramidal neurons (Fig. 6*A*). Epileptiform events were triggered every 5 min, alternating between control trials and trials where Arch was pulsed in PV interneurons throughout the period associated with inhibitory restraint. This experimental design enabled us to perform within-slice statistics. In control trials, the probability of triggering an ED was high, with an average probability of 0.94 ± 0.03. By contrast, when Arch was pulsed in PV interneurons during the period of inhibitory restraint, the chance of successfully evoking EDs was significantly reduced (Fig. 6*A*,*B*). The probability of triggering EDs dropped to 0.68 ± 0.10 during the pulsed-Arch trials ($N = 11$ cells across 11 slices; $W_{(7)} = 1$, $p = 0.03$, two-tailed matched-pairs Wilcoxon signed-rank test).

In cases where an ED was initiated during the pulsed Arch protocol, the onset time relative to the start of NMDA protocol did not differ to control EDs recorded within the same slice (control, 13.7 ± 2.3 s; pulsed Arch, 12.1 ± 2.6 s; $N = 11$ cells across 11 slices; $W_{(11)} = 27$, $p = 0.6377$, two-tailed matched-pairs Wilcoxon signed-rank test; Fig. 6*C*). In addition, the duration of EDs initiated during the pulsed Arch protocol was not different from that of control EDs within the same slice (control, 37.0 ± 7.7 s; pulsed Arch, 56.9 ± 21.2 s; $N = 11$ cells across 11 slices; $W_{(11)} = 25$, $p = 0.5195$, two-tailed matched-pairs Wilcoxon signed-rank test; Fig. 7*A*,*B*), nor was the correlation in ED morphologies (control, $r = 0.55 \pm 0.08$; vs pulsed Arch, $r = 0.64 \pm 0.06$; $N = 12$ cells across 12 slices; $t_{(11)} = 1.723$, $p = 0.1128$, two-tailed paired t test; Fig. 7*A*, *C*). Together, these data support the conclusion that enhancing PV interneuron spiking during the pre-ED period reduces the probability of an ED occurring. And, more broadly, the transition of a network to an epileptiform state can be counteracted by attenuating PV interneuron depolarization block in the face of increasing excitation.

Discussion

Building on previous work (Losi et al., 2010, 2016), our NMDA-evoked *in vitro* model afforded the opportunity to study the recruitment of feedforward inhibitory synaptic processes before seizure-like activity, while providing experimental access to target and manipulate defined neuronal populations. Simultaneous recordings revealed that PV interneuron spiking increases during the period (~20 s) that precedes the onset of the ED, over the same timescale that pyramidal neurons exhibit subthreshold membrane potential and current dynamics consistent with the recruitment of local inhibitory neurons that oppose increasing excitation. At some point, the inhibitory restraint mechanisms are overwhelmed and there is a transient "switch" within the network, such that there is a cessation in PV interneuron spiking and pyramidal neurons start spiking. These findings are in accordance with previous evidence that PV interneurons are strongly recruited in the period preceding epileptiform activity, that PV interneuron spiking activity is transiently interrupted around the onset of epileptiform activity, and that interneurons exhibit particular sensitivity to depolarizing block (Dichter and Spencer, 1969; Trevelyan et al., 2006, 2007; Ziburkus et al., 2006; Losi et al., 2010; Cammarota et al., 2013; Sessolo et al., 2015; Toyoda et al., 2015; Parrish et al., 2019).

Depolarization block reflects the reduced availability of voltage-gated sodium channels, which results from channel inactivation mechanisms. The degree and kinetics of membrane depolarization influence channel inactivation, and previous work has distinguished between fast and slow inactivation mechanisms (Rudy, 1978; Fleidervish et al., 1996; Mickus et al., 1999; Vilin and Ruben, 2001). Fast sodium channel inactivation shows rapid onset on membrane depolarization and underlies the absolute refractory period for action potentials (Hodgkin and Huxley,

1952). Meanwhile, slow sodium channel inactivation emerges following sustained membrane depolarizations, generates cumulative action potential adaptation, and contributes to more prolonged depolarization block effects (Fleidervish et al., 1996; Jung et al., 1997; Mickus et al., 1999; Qian et al., 2014). Slow sodium channel inactivation can also occur at subthreshold membrane potentials, consistent with the idea that the level of background excitation is important (Rudy, 1978; Vilin and Ruben, 2001). At any one moment therefore, the proportion of available voltage-gated sodium channels will reflect a combination of inactivation processes. In the case of a neuron recruited under conditions of increasing network excitability, as occurs before an ED, inactivation mechanisms would be elicited on both a timescale of milliseconds, because of increased spiking, but also on a timescale of seconds, because of sustained levels of membrane depolarization.

Recovery from fast and slow channel inactivation both depend on membrane hyperpolarization (Hodgkin and Huxley, 1952; Fleidervish et al., 1996; Jung et al., 1997). To counteract depolarizing block in PV interneurons, our strategy used trains of brief, optically induced hyperpolarizing pulses, on the basis that this could offer relief from both types of voltage-gated sodium channel inactivation, while still affording the PV interneurons the opportunity to spike. The brief nature of the pulses would be expected to reduce fast inactivation following spiking, meanwhile delivering trains of pulses offers hyperpolarization effects over longer timescales, which can counteract a slow inactivation mechanism (Rudy, 1978; Fleidervish et al., 1996). Consistent with these ideas, the protocol was found to be effective in recovering spiking activity that had been blocked both by somatic current injection and by network hyperexcitability, where the relative contributions of fast and slow inactivation processes are likely to differ.

In the context of our ED model, the light-evoked hyperpolarizing pulses increased the output of PV interneurons on a timescale of seconds, increasing the overall frequency and amplitude of PV interneuron spiking. Our measurements of PV interneuron spiking were made from the soma, and the fidelity with which somatic spikes translate to axonal spikes can vary under conditions of high-frequency stimulation (Jensen and Durand, 2009) and sustained somatic depolarization (Meeks et al., 2005). It was therefore relevant that the membrane potential dynamics of the postsynaptic pyramidal neurons was consistent with increased GABA release, although more direct monitoring of axonal spiking and neurotransmitter release could be explored in the future. In addition to increasing spiking output, the nature of our optogenetic strategy meant that PV interneuron spiking was also modulated on a timescale of milliseconds. It is difficult to fully isolate the importance of spike timing, although neither the timing of the light pulses nor the PV interneuron spikes were related to ED onset on a millisecond timescale. In addition, we established that the pulsed hyperpolarizations did not engage rebound excitation mechanisms, consistent with evidence that hyperpolarization-activated cation channels tend to be recruited at more negative potentials and have little impact on PV interneuron spiking (Aponte et al., 2006). Together, therefore, the data provide strong evidence that a protocol that minimizes depolarizing block is able to increase PV interneuron spike rates and amplitudes across the late pre-ED period, and to reduce the probability of an ED occurring.

It is interesting that the effects on EDs were probabilistic in nature. Such an "all-or-none" effect is consistent with the idea that networks have something akin to a threshold for transitioning into an ED (Jirsa et al., 2014), and that once the network has crossed this threshold, the ED itself represents a regenerative process that is independent of the threshold, most likely involving nonlinear dynamic processes such as recurrent excitatory mechanisms (Anderson et al., 1990; Williams and Dudek, 2007; Jirsa et al., 2014). Once the ED has started, these regenerative mechanisms appear to dominate, determining ED length and morphology, and presumably reducing any further effects of the optogenetic protocol because of pronounced changes in input resistance.

Perhaps most interesting is the fact that the mean ED onset times were similar for the control EDs and for the lower probability EDs that still occurred during the pulsed Arch protocol, suggesting that the network tends to reach ED threshold at similar times. One explanation for this is that the ED onset is reflective of the NMDA dynamics within the slice. Alternatively, the process by which the NMDA protocol causes an ED could involve multiple activity-dependent mechanisms operating in parallel, of which PV interneuron depolarization block is one. These other mechanisms may operate on similar timescales and determine when the network approaches ED threshold. For instance, the buildup of extracellular potassium because of increased spiking activity levels and/or intense subthreshold synaptic activity could move a network closer to its ED threshold (Jirsa et al., 2014). Indeed, there could be trade-offs within the system, in the sense that while the pulsed Arch protocol may tend to draw the network away from ED threshold by reducing PV interneuron depolarization block, the protocol and associated spiking could also enhance mechanisms that nudge the network toward ED threshold, such as by causing further increases in extracellular potassium or even effects on local proton gradients associated with Arch itself (Chow et al., 2010; El-Gaby et al., 2016).

The membrane potential dynamics associated with the gradual and increasing recruitment of feedforward inhibitory restraint mechanism may be particularly conducive to eliciting a combination of slow and fast inactivation of voltage-gated sodium channels (Trevelyan et al., 2006, 2007; Cammarota et al., 2013). Indeed, the optical rescue of depolarization block was evident during the later stages of the inhibitory restraint window, when the PV interneurons have experienced a period of sustained membrane depolarization and are spiking at higher rates. However, it seems likely that different networks and patterns of preseizure activity will generate varying degrees and combinations of channel inactivation. For instance, depolarization block is itself influenced by levels of extracellular potassium, and therefore the kinetics of channel inactivation may vary depending on how different network dynamics influence extracelular ion concentrations (Shin et al., 2010). Equally, depolarization block may be less limiting in some networks, where processes such as the depletion of GABA-containing vesicles or the overwhelming of postsynaptic regulatory mechanisms, may represent key factors in the loss of inhibitory control (Fujiwara-Tsukamoto et al., 2010; Zhang et al., 2012). It will therefore be interesting to examine these processes in different seizure models, including spontaneous epileptiform activity, where one could imagine using closed-loop optogenetics to counteract the effects of depolarization block (Krook-Magnuson et al., 2013).

Our findings are consistent with evidence that epileptiform activity is disrupted by optogenetically or chemogenetically enhancing the output of PV interneurons (Krook-Magnuson et al., 2013; Sessolo et al., 2015; Shiri et al., 2017; Călin et al., 2018; Lévesque et al., 2019). At the same time, other work has shown that interneurons can exert proepileptic effects. This partly

reflects diversity among interneuron populations (Khoshkhoo et al., 2017), but PV interneurons have been directly implicated in initiating seizure-like activity, particularly under conditions in which interneuronal synchronization of the network is enhanced. For instance, channelrhodopsin-expressing PV interneurons can increase the probability of eliciting an epileptiform event when activated selectively within the excitatory focus (Sessolo et al., 2015), when activated in the absence of excitatory synaptic transmission (Bohannon and Hablitz, 2018), or when using repeated activation protocols (Shiri et al., 2016; Lévesque et al., 2019). These studies highlight the complex interplay between the processes that influence PV interneuron output. It will therefore be interesting to examine the contribution of depolarizing block mechanisms under different conditions, including where experimental manipulations can themselves contribute to depolarization block, as has been shown for channelrhodopsin-expressing interneurons (Herman et al., 2014). A further challenge will be how we improve methods for circuit control. One could imagine pharmacological strategies both to enhance endogenous hyperpolarizing mechanisms via potassium channels and to counteract the slow inactivation of voltage-gated sodium channels. Similarly, one could imagine improving exogenous strategies by targeting hyperpolarizing tools to the most relevant subcellular compartments, or by combining strategies to increase PV interneuron recruitment, while also counteracting the rate-limiting processes associated with increased excitation (Călin et al., 2018; Magloire et al., 2019).

References

Anderson WW, Stasheff SF, Swartzwelder HS, Wilson WA (1990) Regenerative, all-or-none electrographic seizures in the rat hippocampal slice in Mg-free and physiological medium. Brain Res 532:288–298.

Aponte Y, Lien C-C, Reisinger E, Jonas P (2006) Hyperpolarization-activated cation channels in fast-spiking interneurons of rat hippocampus. J Physiol 574:229–243.

Bartos M, Elgueta C (2012) Functional characteristics of parvalbumin- and cholecystokinin-expressing basket cells. J Physiol 590:669–681.

Berdichevsky Y, Dzhala V, Mail M, Staley KJ (2012) Interictal spikes, seizures and ictal cell death are not necessary for post-traumatic epileptogenesis in vitro. Neurobiol Dis 45:774–785.

Bohannon AS, Hablitz JJ (2018) Optogenetic dissection of roles of specific cortical interneuron subtypes in GABAergic network synchronization. J Physiol 596:901–919.

Călin A, Stancu M, Zagrean A-M, Jefferys JGR, Ilie AS, Akerman CJ (2018) Chemogenetic recruitment of specific interneurons suppresses seizure activity. Front Cell Neurosci 12:293.

Cammarota M, Losi G, Chiavegato A, Zonta M, Carmignoto G (2013) Fast spiking interneuron control of seizure propagation in a cortical slice model of focal epilepsy. J Physiol 591:807–822.

Chow BY, Han X, Dobry AS, Qian X, Chuong AS, Li M, Henninger MA, Belfort GM, Lin Y, Monahan PE, Boyden ES (2010) High-performance genetically targetable optical neural silencing by light-driven proton pumps. Nature 463:98–102.

Curtis DR, Duggan AW, Felix D, Johnston G. a R (1970) GABA, bicuculline and central inhibition. Nature 226:1222–1224.

De Simoni A, Griesinger CB, Edwards FA (2003) Development of rat CA1 neurones in acute versus organotypic slices: role of experience in synaptic morphology and activity. J Physiol 550:135–147.

Di Cristo G, Wu C, Chattopadhyaya B, Ango F, Knott G, Welker E, Svoboda K, Huang ZJ (2004) Subcellular domain-restricted GABAergic innervation in primary visual cortex in the absence of sensory and thalamic inputs. Nat Neurosci 7:1184–1186.

Dichter MA, Ayala GF (1987) Cellular mechanisms of epilepsy: a status report. Science 237:157–164.

Dichter M, Spencer WA (1969) Penicillin-induced interictal discharges from the cat hippocampus. II. Mechanisms underlying origin and restriction. J Neurophysiol 32:663–687.

Dyhrfjeld-Johnsen J, Berdichevsky Y, Swiercz W, Sabolek H, Staley KJ (2010) Interictal spikes precede ictal discharges in an organotypic hippocampal slice culture model of epileptogenesis. J Clin Neurophysiol 27:418–424.

El-Gaby M, Zhang Y, Wolf K, Schwiening CJ, Paulsen O, Shipton OA (2016) Archaerhodopsin selectively and reversibly silences synaptic transmission through altered pH. Cell Rep 16:2259–2268.

Ellender TJ, Raimondo JV, Irkle A, Lamsa KP, Akerman CJ (2014) Excitatory effects of parvalbumin-expressing interneurons maintain hippocampal epileptiform activity via synchronous afterdischarges. J Neurosci 34:15208–15222.

Fleidervish IA, Friedman A, Gutnick MJ (1996) Slow inactivation of Na+ current and slow cumulative spike adaptation in mouse and guinea-pig neocortical neurones in slices. J Physiol 493:83–97.

Freund TF, Buzsáki G (1996) Interneurons of the hippocampus. Hippocampus 6:347–470.

Fujiwara-Tsukamoto Y, Isomura Y, Imanishi M, Ninomiya T, Tsukada M, Yanagawa Y, Fukai T, Takada M (2010) Prototypic seizure activity driven by mature hippocampal fast-spiking interneurons. J Neurosci 30:13679–13689.

Galarreta M, Hestrin S (1999) A network of fast-spiking cells in the neocortex connected by electrical synapses. Nature 402:72–75.

Gibson JR, Beierlein M, Connors BW (1999) Two networks of electrically coupled inhibitory neurons in neocortex. Nature 402:75–79.

Han X, Chow BY, Zhou H, Klapoetke NC, Chuong A, Rajimehr R, Yang A, Baratta MV, Winkle J, Desimone R, Boyden ES (2011) A high-light sensitivity optical neural silencer: development and application to optogenetic control of non-human primate cortex. Front Syst Neurosci 5:18.

Herman AM, Huang L, Murphey DK, Garcia I, Arenkiel BR (2014) Cell type-specific and time-dependent light exposure contribute to silencing in neurons expressing Channelrhodopsin-2. eLife 3:e01481.

Hodgkin AL, Huxley AF (1952) A quantitative description of membrane current and its application to conduction and excitation in nerve. J Physiol 117:500–544.

Ilie A, Raimondo JV, Akerman CJ (2012) Adenosine release during seizures attenuates $GABA_A$ receptor-mediated depolarization. J Neurosci 32:5321–5332.

Jensen AL, Durand DM (2009) High frequency stimulation can block axonal conduction. Exp Neurol 220:57–70.

Jirsa VK, Stacey WC, Quilichini PP, Ivanov AI, Bernard C (2014) On the nature of seizure dynamics. Brain J Brain 137:2210–2230.

Jung HY, Mickus T, Spruston N (1997) Prolonged sodium channel inactivation contributes to dendritic action potential attenuation in hippocampal pyramidal neurons. J Neurosci 17:6639–6646.

Khoshkhoo S, Vogt D, Sohal VS (2017) Dynamic, cell-type-specific roles for GABAergic interneurons in a mouse model of optogenetically inducible seizures. Neuron 93:291–298.

Krook-Magnuson E, Armstrong C, Oijala M, Soltesz I (2013) On-demand optogenetic control of spontaneous seizures in temporal lobe epilepsy. Nat Commun 4:1376.

Lévesque M, Chen L-Y, Etter G, Shiri Z, Wang S, Williams S, Avoli M (2019) Paradoxical effects of optogenetic stimulation in mesial temporal lobe epilepsy. Ann Neurol 86:714–728.

Losi G, Cammarota M, Chiavegato A, Gomez-Gonzalo M, Carmignoto G (2010) A new experimental model of focal seizures in the entorhinal cortex. Epilepsia 51:1493–1502.

Losi G, Marcon I, Mariotti L, Sessolo M, Chiavegato A, Carmignoto G (2016) A brain slice experimental model to study the generation and the propagation of focally-induced epileptiform activity. J Neurosci Methods 260:125–131.

Magloire V, Cornford J, Lieb A, Kullmann DM, Pavlov I (2019) KCC2 overexpression prevents the paradoxical seizure-promoting action of somatic inhibition. Nat Commun 10:1225.

Meeks JP, Jiang X, Mennerick S (2005) Action potential fidelity during normal and epileptiform activity in paired soma-axon recordings from rat hippocampus. J Physiol 566:425–441.

Mickus T, Jung H-Y, Spruston N (1999) Slow Sodium Channel Inactivation in CA1 Pyramidal Cells. Ann N Y Acad Sci 868:97–101.

Owen SF, Liu MH, Kreitzer AC (2019) Thermal constraints on in vivo optogenetic manipulations. Nat Neurosci 22:1061–1065.

Parrish RR, Codadu NK, Scott CM-G, Trevelyan AJ (2019) Feedforward inhibition ahead of ictal wavefronts is provided by both parvalbumin and somatostatin expressing interneurons. J Physiol 597:2297–2314.

Pawelzik H, Hughes DI, Thomson AM (2002) Physiological and morphological diversity of immunocytochemically defined parvalbumin- and cholecystokinin-positive interneurones in CA1 of the adult rat hippocampus. J Comp Neurol 443:346–367.

Qian K, Yu N, Tucker KR, Levitan ES, Canavier CC (2014) Mathematical analysis of depolarization block mediated by slow inactivation of fast sodium channels in midbrain dopamine neurons. J Neurophysiol 112:2779–2790.

Rudy B (1978) Slow inactivation of the sodium conductance in squid giant axons. Pronase resistance. J Physiol 283:1–21.

Schevon CA, Weiss SA, McKhann G Jr, Goodman RR, Yuste R, Emerson RG, Trevelyan AJ (2012) Evidence of an inhibitory restraint of seizure activity in humans. Nat Commun 3:1060.

Sessolo M, Marcon I, Bovetti S, Losi G, Cammarota M, Ratto GM, Fellin T, Carmignoto G (2015) Parvalbumin-positive inhibitory interneurons oppose propagation but favor generation of focal epileptiform activity. J Neurosci 35:9544–9557.

Shin DS-H, Yu W, Fawcett A, Carlen PL (2010) Characterizing the persistent CA3 interneuronal spiking activity in elevated extracellular potassium in the young rat hippocampus. Brain Res 1331:39–50.

Shiri Z, Manseau F, Lévesque M, Williams S, Avoli M (2016) Activation of specific neuronal networks leads to different seizure onset types. Ann Neurol 79:354–365.

Shiri Z, Lévesque M, Etter G, Manseau F, Williams S, Avoli M (2017) Optogenetic low-frequency stimulation of specific neuronal populations abates ictogenesis. J Neurosci 37:2999–3008.

Somogyi P, Klausberger T (2005) Defined types of cortical interneurone structure space and spike timing in the hippocampus. J Physiol 562:9–26.

Stoppini L, Buchs P-A, Muller D (1991) A simple method for organotypic cultures of nervous tissue. J Neurosci Methods 37:173–182.

Streit P, Thompson SM, Gähwiler BH (1989) Anatomical and physiological properties of GABAergic neurotransmission in organotypic slice cultures of rat hippocampus. Eur J Neurosci 1:603–615.

Stujenske JM, Spellman T, Gordon JA (2015) Modeling the spatiotemporal dynamics of light and heat propagation for in vivo optogenetics. Cell Rep 12:525–534.

Toyoda I, Fujita S, Thamattoor AK, Buckmaster PS (2015) Unit activity of hippocampal interneurons before spontaneous seizures in an animal model of temporal lobe epilepsy. J Neurosci 35:6600–6618.

Trevelyan AJ, Schevon CA (2013) How inhibition influences seizure propagation. Neuropharmacology 69:45–54.

Trevelyan AJ, Sussillo D, Watson BO, Yuste R (2006) Modular propagation of epileptiform activity: evidence for an inhibitory veto in neocortex. J Neurosci 26:12447–12455.

Trevelyan AJ, Sussillo D, Yuste R (2007) Feedforward inhibition contributes to the control of epileptiform propagation speed. J Neurosci 27:3383–3387.

Vilin YY, Ruben PC (2001) Slow inactivation in voltage-gated sodium channels. Cell Biochem Biophys 35:171–190.

Williams PA, Dudek FE (2007) A chronic histopathological and electrophysiological analysis of a rodent hypoxic-ischemic brain injury model and its use as a model of epilepsy. Neuroscience 149:943–961.

Zhang ZJ, Koifman J, Shin DS, Ye H, Florez CM, Zhang L, Valiante TA, Carlen PL (2012) Transition to seizure: ictal discharge is preceded by exhausted presynaptic GABA release in the hippocampal CA3 region. J Neurosci 32:2499–2512.

Ziburkus J, Cressman JR, Barreto E, Schiff SJ (2006) Interneuron and pyramidal cell interplay during in vitro seizure-like events. J Neurophysiol 95:3948–3954.